Journal of Constructional Steel Research 199 (2022) 107622

Contents lists available at ScienceDirect

Journal of Constructional Steel Research

journal homepage: www.elsevier.com/locate/jcsr

Experimental cyclic response of rubberised concrete-filled steel tubes

A.Y. Elghazouli [a], A. Mujdeci [a], D.V. Bompa [a,b], Y.T. Guo [a,c,*]

[a] Department of Civil and Environmental Engineering, Imperial College London, UK
[b] Department of Civil and Environmental Engineering, University of Surrey, UK
[c] Institute for Ocean Engineering, Tsinghua Shenzhen International Graduate School, China

ARTICLE INFO

Keywords:
Concrete filled steel tubes
Rubberised concrete
Inelastic cyclic response
Hysteretic behaviour
Ductility and energy dissipation

ABSTRACT

This paper examines the behaviour of circular steel tubes infilled with concrete incorporating recycled rubber particles. The rubberised concrete-filled steel tubes are tested under lateral cyclic deformations with and without co-existing axial loading. A detailed account of the cyclic tests on twelve specimens is provided together with complementary material and section tests. The rubber replacement ratio is varied up to a relatively high value of 60%, under axial loads reaching up to 30% of the nominal capacity. Hollow steel members are also tested for comparison purposes. The experimental results are discussed in detail with respect to the member stiffness, capacity, ductility, energy dissipation and failure mechanisms. Although high rubber ratios lead to a considerable loss in concrete strength, the test results show that the corresponding reduction in member capacity is much less significant due to the contribution of the steel tube and the comparatively high confinement effects mobilised within the rubberised concrete. In comparison with the members incorporating normal concrete, the rubberised concrete members are found to exhibit up to about 10% and 17% increase in ductility and energy dissipation, respectively, depending on the rubber content. Analytical treatments are then used to suggest simplified relationships for predicting the stiffness, moment-axial strength interaction, plastic hinge length and local ductility criteria. Overall, the test results demonstrate the favourable inelastic cyclic performance of circular steel tubes infilled with rubberised concrete and provide valuable experimental data. The proposed expressions for key response parameters also offer the basis for developing practical assessment and design methods.

1. Introduction

Used tyres pose significant waste management issues due to inadequate disposal methods and represent a hazard to human health and to the environment [1,2]. An attractive solution is incorporating recycled rubber in concrete, as a replacement for mineral aggregates, to obtain rubberised concrete (RuC) [3]. Despite its potential benefits in terms of ductility and energy absorption, the main drawback of incorporating rubber particles in concrete is the inherently lower strength of RuC compared to conventional concrete (CC) [4]. However, the relatively low RuC strength can be offset by providing external confinement which, combined with the high ductility and energy absorption of rubber particles, can provide characteristics suitable for seismic design applications [5].

Reinforced rubberised concrete (RRuC) members exhibit a reduction in compressive strength but can provide an increase in energy dissipation by up to 150% in comparison with CC elements [6]. Tests on reinforced concrete (RC) beams and columns with 18% rubber content indicated member strength reductions of 6%–12% depending in the reinforcement ratio, while the material strength was reduced by 31% [7,8]. Cyclic tests on RRuC showed that although greater ductility is obtained at relatively high rubber ratios, the loss in member capacity becomes significant above 20% rubber content [9].

Previous studies have shown that RRuC members provided with external confinement, through fibre reinforced polymer (FRP) sheets and/or steel sections, offered relatively high levels of energy dissipation and improved capacity [10–12]. Combined monotonic compression and bending tests, up to 60% rubber ratio, showed that FRP confinement provides improved capacity and higher rotation capacity compared with RRuC with internal stirrup confinement [4,13]. This was also confirmed by cyclic tests on FRP-confined RRuC up to 60% rubber ratio, which showed a good balance between bending capacity and ductility compared with RC members [14].

Compression tests on circular, square and rectangular RuC-filled

* Corresponding author at: Department of Civil and Environmental Engineering, Imperial College London, UK.
E-mail addresses: a.elghazouli@imperial.ac.uk (A.Y. Elghazouli), a.mujdeci18@imperial.ac.uk (A. Mujdeci), d.bompa@surrey.ac.uk (D.V. Bompa), guoyutao@sz.tsinghua.edu.cn, yutao.guo@imperial.ac.uk (Y.T. Guo).

https://doi.org/10.1016/j.jcsr.2022.107622
Received 9 August 2022; Received in revised form 5 October 2022; Accepted 11 October 2022

sections with up to 15% rubber, showed that ductility increased by 40% to 150% in proportion to the rubber ratio and as a function of the section type [15,16]. Circular tubes allow higher confinement effects to develop in the concrete core, in comparison with square or rectangular forms [17,18]. Enhanced ductility and energy dissipation were also obtained under axial compression, in single and double-skin square tubular members filled using concrete with 30% replacement [19,20]. Eccentric tests on RuCFST with 30% rubber ratio indicated improved bending performance and ductility in RuCFSTs and superior capacity for circular sections compared to square counterparts [21].

Combined monotonic axial and bending tests on rubberised concrete filled steel tubes (RuCFSTs) with rubber ratios up to 60%, showed that whilst the capacity is reduced with the increase in the rubber ratio, an enhanced confinement action is obtained for high content RuC concrete compared with CC materials [22]. Cyclic RuCFST cantilever tests with up to 15% rubber content, indicated that 5% rubber gives the lowest decrease, of 5%, in the cyclic strength and the highest increase in the ductility, by 52% compared to CFST counterparts [23]. Square RuC-filled tubes with up to 5% rubber had comparable cyclic behaviour to conventional CFST members confirming the suitability of such RuCFST as structural components [24].

Monotonic and cyclic tests on circular, square and rectangular RuCFSTs with a rubber ratio of up to 15% showed that existing codes are conservative in predicting the capacity of the tested specimens, while the current cross-section slenderness limits could be relaxed [11,25]. Similar observations were made in other tests with low rubber ratios [26]. For high rubber ratios up to 60%, codes tend to provide unconservative estimates for the axial compression capacity of RuCFST and relatively conservative predictions of the flexural capacity of RuCFST in bending only [22].

Although some of the above studies assessed the general suitability of RuCFST members in inelastic loading conditions, these were limited to rubber ratios below 15% and axial load ratios below 20% [11,24,25,27,28]. As noted above, tests under monotonic compression and/or flexural loading showed a reliable structural performance for rubber contents around and above 30% [21,22]. Provided adequate assessment and quantification are carried out, it is expected that a relatively high rubber content, beyond the values considered in previous cyclic tests, would provide both a reliable structural performance as well as an improved environmental solution. There is also a need for a detailed evaluation of the underlying local failure mechanisms, which involve intricate inelastic interactions between the steel and concrete constituents. Moreover, as the rubberised concrete properties extend beyond the scope of current code methods, they are unable to predict reliably the strength of RuCFST, and expressions to quantify the main inelastic design parameters for such members are lacking.

This paper examines the inelastic cyclic response of RuCFST members incorporating rubber ratios as high as 60% of aggregate replacement, and under axial loading reaching up to 30% of the cross-section compression capacity. The test results provide a detailed insight into the main response characteristics, including the stiffness, strength, ductility, plastic hinge length, local buckling, and energy dissipation of RuCFST as a function of rubber content and axial load. Analytical assessments are carried out and simplified expressions are proposed for predicting the key inelastic response parameters in support of practical assessment and design approaches.

2. Experimental programme

2.1. Specimen details

As shown in Table 1, the cyclic test series included 12 hollow steel (ST) and concrete-filled (CF) circular tubes, with varying volumetric rubber ratios (ρ_{vr}) of 0, 0.3 and 0.6 (denoted R00, R30, R60), and three different axial load ratios (referred to as n_0, n_1 and n_2) representing about 0%, 15%, 30% of the estimated cross-section capacity. The axial loads n_0 specimens had very small axial loads in actual tests, which were imposed during the specimen installation to ensure appropriate positioning and loading. The specimens are labelled following the convention of specimen type (ST or CF), rubber content (R00, R30 or R60) and applied co-existing axial load level (n_0, n_1 or n_2). All the specimens were tested as vertical cantilever members with a nominal length of 1200 mm, with a cross-sectional outer diameter of 152 mm and a thickness of 2.8 mm. The diameter-to-thickness ratio of the tube specimens was selected such that the steel could develop full yielding before the onset of local buckling, as required in ductile seismic design. The length of the specimens was also selected such that global instability would not occur or influence the response. Clearly, situations in which the member geometry is such that elastic local buckling occurs, or global member buckling affects the response, are beyond the scope of this study and would require further experimental or numerical investigations. Also, this study focuses on the behaviour of RuCFSTs with circular cross-sections. Other shapes, such as those with rectangular cross-sections, would have different confinement properties and would need further investigation. Two additional steel plates of 10 mm thickness were welded to the two ends of the specimens. The bottom end was closed while the top end was open for concrete casting. Although geometrical imperfections were not mapped, it was found in an ongoing complementary numerical study that, in this geometric range, imperfections do not notably influence the response nor failure modes of these members in bending-dominated cases.

Table 1
Specimen details.

Specimen ID	Size ($D \times L_c$) / t (mm × mm/mm)	ρ_{vr}	n_i	N (kN)
STn_0	152 × 1200 / 2.8	–	0	4.8
STn_1	152 × 1200 / 2.8	–	0.15	66.8
STn_2	152 × 1200 / 2.8	–	0.30	134.8
CFR00n_0	152 × 1195 / 2.8	0	0	7.1
CFR30n_0	152 × 1190 / 2.8	0.30	0.15	6.4
CFR60n_0	152 × 1217 / 2.8	0.60	0.30	8.0
CFR00n_1	152 × 1195 / 2.8	0	0	288.4
CFR30n_1	152 × 1200 / 2.8	0.30	0.15	136.9
CFR60n_1	152 × 1200 / 2.8	0.60	0.30	102.5
CFR00n_2	152 × 1195 / 2.8	0	0	592.9
CFR30n_2	152 × 1197 / 2.8	0.30	0.15	277.9
CFR60n_2	152 × 1197 / 2.8	0.60	0.30	211.7

2.2. Material properties

The concrete infill incorporated three different rubber content ratios, referred to as R00, R30, R60, and corresponding to 0%, 30%, and 60%, respectively, as a replacement of both fine and coarse mineral aggregates by volume. The concrete mix proportions are given in Table 2. All concrete mixes included 340 kg/m^3 CEM I 52.5R cement to BS EN 197–1 [29], and 85 kg/m3 fly ash Category N to BS EN 450–1 [30], with a

Table 2
Concrete mixes.

Component	R00	R30	R60
Cement (kg)	340	340	340
Fly ash (kg)	85	85	85
Aggregates(kg)			
—0–5 mm	820	574	328
—5–10 mm	1001	700.7	400.4
Rubber (kg)			
—0–4.0 mm	–	74.3	148.5
—4.0–10.0 mm	–	16.5	33
—10–20.0 mm	–	74.25	148.5
Admixture(l)			
—(PL + SPL)	7.6	7.6	7.6
w/c	0.35	0.35	0.35

* PL plasticizer, SPL super plasticizer, w/c water cement ratio.

specific gravity (SG) of 3.10 and 2.33, respectively. Sand with a particle size up to 5 mm, a moisture content of around 5% and SG of 2.65, as well as gravel with a particle size of 5–10 mm, moisture content of 3% and SG of 2.65, were used. A rubber blend consisting of particle sizes of 0–4 mm, 4–10 mm and 10–20 mm was added to replace both sand and gravel. The rubber particles were obtained from two sources [31]. Rubber aggregates up to 10 mm in diameter, were produced from car tyre recycling. The larger rubber particles were produced from truck or bus tyre recycling, with typically higher density than car tyre particles. All rubber particles were reported to have 25% content of carbon black, polymers in the range of 40–55%, whereas the remaining constituents are softeners and fillers. The specific gravity of rubber was 1.1, whereas the water absorption 7.1% for 4–10 mm particles and 1.05 for 10–20 mm particles.

Using a 250-l mixer, a dry mix of sand and gravel was firstly mixed for 1 min, which was followed by the rubber blend and the binders and mixed for 3–5 min until homogenous. The dry constituents were then mixed with half of the water for another 2–3 min. Finally, the remaining water and admixtures were added in the container and mixed for up to another 5 min, until a wet homogenous mixture was obtained. The fresh concrete was either poured in cubic and cylindrical forms, or in the circular steel tubes. The concrete in the forms was compacted on a vibrating table, whilst a concrete poker was employed for the tubes to remove entrapped air bubbles.

Standard tensile coupon tests were carried out to determine the stress–strain characteristics of steel from the tubes, which were all from the same batch. Based on the average of at least three coupons, the 0.2% steel proof yield strength f_s was 295 MPa, the ultimate steel strength f_u was 395 MPa, the ultimate strain ε_u was 0.18. On the other hand, for concrete, the compressive strength from cylinders (f_{rc}) and cubes ($f_{rc,cube}$), at 28 days and on the testing day, are listed in Table 3. The concrete with the same rubber ratios used identical mixes, and the average values of at least 9 material tests (cubes and cylinders respectively) are given in Table 3. The standard deviations in all cases were less than 5%. The typical stress-strain curves for concrete in compression and steel in tension are depicted in Fig. 1. The material properties were similar to those obtained in previous studies [22,31]. The elastic modulus and compressive strength reduce as the rubber ratio increases, while the post-peak ductility is enhanced.

In addition to the material characterization tests on steel and concrete, complementary stub-column tests were undertaken to evaluate the actual composite cross-sectional axial compressive capacity. The results of CFST stub columns of 300 mm as well as 600 mm length, using the same concrete employed in the cyclic test specimens, are given in Table 4. As shown in the table, the short specimens referred to by *S* (i.e. $L_c/D \approx 2$), and the longer specimens denoted with *L* (i.e. $L_c/D \approx 4$) had virtually the same axial capacity. The results of the axially loaded specimens are similar to those obtained in previous studies [22].

2.3. Testing arrangement and instrumentation

The cyclic tests were carried out on cantilever specimens subjected to a combination of a constant vertical load and gradually increasing lateral cyclic displacements, as shown in the setup in Fig. 2. The lateral cyclic displacements were applied using a horizontally placed hydraulic actuator with a capacity of 250 kN and a stroke of ±125 mm stroke, while the vertical load was applied using a 500 kN actuator. Load cells were directly mounted on both actuators, and out-of-plane restraints were employed. The base plate of the test specimen was bolted to a very stiff foundation plate (600x600x50 mm) at the base, hence ensuring fixed-end cantilever boundary conditions.

An arrangement of hinges was used at both ends of the actuators as shown in Fig. 2. For the vertical actuator, the distance between the two hinges was 1443 mm, leading to a maximum rotation θ up to 0.08 rad. While the actuator load *N* was kept constant through the test, the change (1-cos θ) in vertical load at the maximum rotation of the loading beam would be less than 0.32%. Therefore, the axial load in the vertical direction remains virtually constant. However, the horizontal component, which is more significant, is accounted for when determining the lateral loading, as discussed in the next section.

After applying and maintaining the constant vertical load (*N*), the lateral cyclic displacement histories were applied following the widely-adopted ECCS [32] procedure. Based on an estimated yield displacement δ_y of 8.0 mm, one cycle was applied at $0.25\delta_y$, $0.50\delta_y$, $0.75\delta_y$, $1.0\delta_y$, followed by three full cycles at each displacement level of $(2n + 2)\delta_y$ (with $n = 0,1,2,3,4\ldots$) until failure occurred or the horizontal actuator stroke was reached. The displacements were applied at a control rate of about 0.2 mm/min on average.

As shown in Fig. 3, strain gauges were placed within the bottom 250 mm length of the specimen at the outmost fibres on both sides along the loading direction. The lateral and vertical displacements were measured using LVDTs and string pots, and the rotations were monitored using seven inclinometers attached to the specimens and hydraulic jacks. Importantly, in addition, a Digital Image Correlation (DIC) system was employed to measure the detailed local deformations and strains within the expected plastic hinge zone of the specimens.

Table 3
Concrete properties from material tests.

Concrete type	Concrete strength			
	at 28 days		at testing	
	f_{rc} (MPa)	$f_{rc,cube}$ (MPa)	f_{rc} (MPa)	$f_{rc,cube}$ (MPa)
CFR00n_{0-2}	69.6	81.5	81.4	91.7
CFR30n_{0-2}	18.2	33.2	18.9	34.8
CFR60n_{0-2}	5.8	8.1	6.6	10.7

* f_{rc} refers to normal concrete if rubber ratio is 0.

3. Test results and observations

3.1. Member behaviour

With reference to the experimental set-up in Fig. 2 as well as the force diagram shown in Fig. 4, and accounting for the 2nd order *P*-Δ effect, the overall moment *M* at the fixed end of the specimen can be determined as:

$$M = N(L_c + L_d + L_t)sin\theta + V_A L_c \quad (1)$$

where *N* is the axial force, L_c is the length of the member, L_d is the distance between the member top and the lower vertical hinge, L_t is the distance between the two vertical hinges, θ is the rotation, and V_A is the applied horizontal force from the lateral actuator.

The second order *P*-Δ moment ($M_{P-\Delta}$), can also be represented as:

$$M_{P-\Delta} = N\delta_c cos\theta \approx N\delta_c \quad (2)$$

where δ_C is horizontal displacement at the top the of the specimen.

Accordingly, the overall horizontal force, which represents the effective lateral seismic load V_H applied at the top of the member, may be determined as:

$$V_H = \frac{M - M_{P-\Delta}}{L_c} \approx V_A + \frac{N(L_c + L_d + L_t)sin\theta - N\delta_c}{L_c} \quad (3)$$

Using the above equations, the fixed end moment *M* and equivalent seismic force V_H are plotted against the specimen horizonal displacement δ_C in Fig. 5 and Fig. 6, respectively. Since all specimens had a length of 1200 mm, the drift ratio could be directly determined as δ_c/1200. On the other hand, Fig. 7 and Fig. 8 show views of the plastic hinge regions of the hollow steel (ST) and concrete-infilled (CF) specimens, respectively, after the tests, while Fig. 9 shows the infill concrete after careful removal of the steel tubes following the tests.

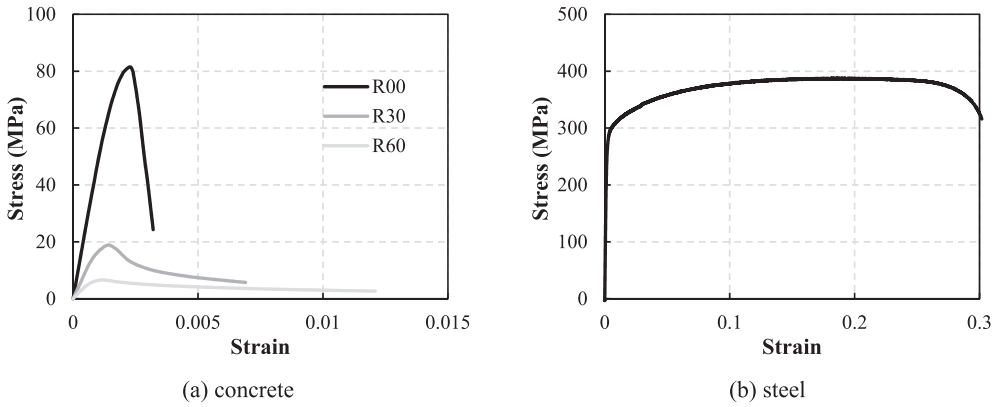

Fig. 1. Stress-strain response from material tests.

Table 4
Axial loaded stub column tests.

Specimen ID	Size ($D \times L$) / t (mm × mm/mm)	ρ_{vr}	f_{rc}	N (kN)
CFR00S	152 × 300 / 2.8	0	81.4	1944
CFR30S	152 × 300 / 2.8	0.30	18.9	856
CFR60S	152 × 300 / 2.8	0.60	6.6	597
CFR00L	152 × 600 / 2.8	0	81.4	1929
CFR30L	152 × 600 / 2.8	0.30	18.9	866
CFR60L	152 × 600 / 2.8	0.60	6.6	551

By examining the cyclic moment behaviour in Fig. 5 (which captures the overall member response without the second order-related lateral load reduction present in Fig. 6), it is evident that the three hollow (ST) specimens generally exhibited poor hysteretic performance compared to the infilled (CF) members. Even without axial loading, the cyclic degradation was severe in the ST members due to the early onset of local buckling. In contrast, the presence of the concrete infill in the CF specimens led to a significant delay in the initiation of local buckling, resulting in a more stable hysteretic behaviour. More detailed discussions of the local buckling effects in the ST and CF members are provided in Section 3.2 below.

Comparing the moment response of the nine CF members in Fig. 5, it is shown that the R00 (normal concrete infill) specimens had relatively more pinching in the cyclic response compared to the rubberised concrete (R30 and R60) specimens, which was more pronounced under high axial loading. These cyclic deterioration effects have a direct influence on the energy dissipation capacity of the member, as discussed in more detail in Section 4 below.

The typical failure patterns of the CF specimens, shown in Fig. 8 and Fig. 9, involved outward local buckling at the base, followed by fracture after a few additional cycles. The rubberised concrete appeared to be as effective as the normal concrete in delaying local buckling within the expected plastic hinge region. As expected, when a high axial load was applied, the extent of the concrete damaged areas was larger.

In order to provide a more direct comparison between the behaviour of various specimens, the envelopes of the cyclic responses are combined in Fig. 10 which illustrates the influence of the axial load, and Fig. 11 which illustrates the influence of the rubber content. Clearly, the moment or lateral load capacity is a function of axial load as well as the reduction in concrete strength, depending on the strength interaction characteristics, which will be discussed in detail in Section 4. The figures also show that the axial load and the rubber content have an influence on the member stiffness as well as the post-peak ductility characteristics, as discussed further in subsequent sections.

3.2. Main response parameters

The key response parameters for the 12 cyclic tests are summarized in Table 5. The first of these is the member stiffness k_{test}. Using the

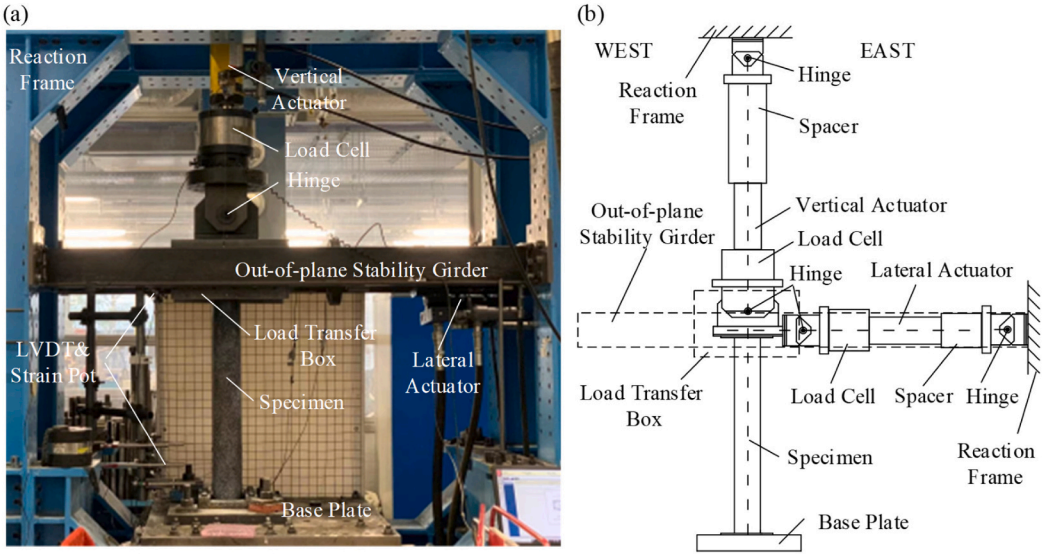

Fig. 2. Cyclic test setup: (a) view of test rig, (b) schematic of testing arrangement.

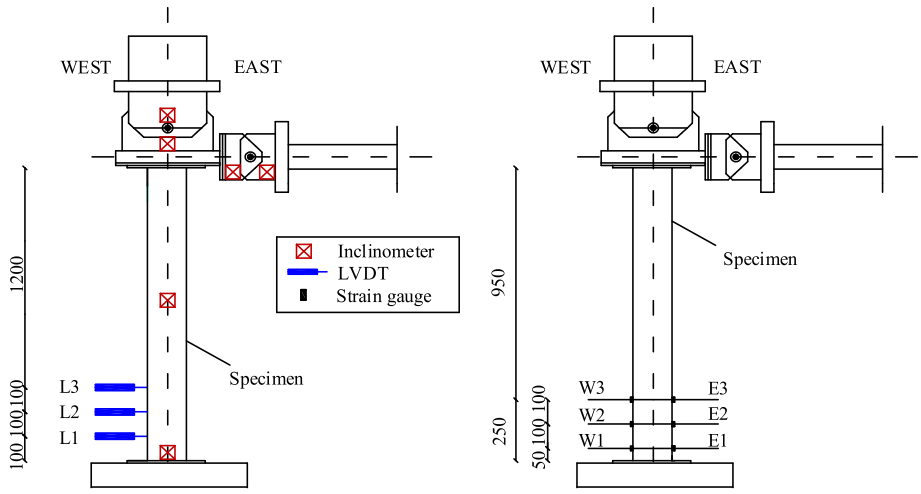

Fig. 3. Instrumentation details.

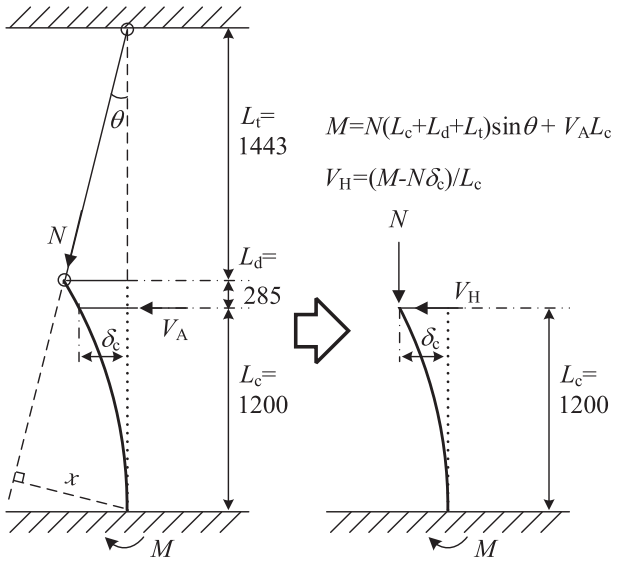

Fig. 4. Force diagram of the member.

procedure adopted in previous studies on CFST members [33,34], this is considered herein as the secant stiffness at 40% of the peak moment. As shown in Table 5 as well as in Fig. 10 and Fig. 11, the member stiffness generally increased with axial loads and decreased with higher rubber contents. For CF members, on average, the stiffness increased by 17.3% from n_0 to n_1, and by 20.6% from n_0 to n_2. On the other hand, the stiffness decreased by 12.1% from R00 to R30, and by 29.3% from R00 to R60.

Although several methods can be used for estimating the yield point in various composite members [35], it is assumed herein to correspond to the intersection between the secant stiffness, as described above, and horizontal line at the peak capacity of the response envelope. Using this procedure, the derived yield displacement δ_y as well as the corresponding load V_y and moment M_y are listed in Table 5.

For the member capacity, V_{peak} and M_{peak} in Table 5 refer to the maximum load and maximum moment in the envelope curves, while δ_{Vpeak} and δ_{Mpeak} are the corresponding displacements, respectively. M_{peak} decreased by 12.8%, 20.1%, 27.2% from R00 to R30 for each axial load level (i.e. for n_0, n_1, n_2, respectively), and by 22.3%, 33.6%, 38.9% from R00 to R60. On the other hand, V_{peak} decreased by 12.1%, 10.1%, 15.9% from R00 to R30 for each axial load level, and by 21.9%, 25.7%, 30.1% from R00 to R60. From R00 to R30, the loss in capacity was not severe since the enhanced confinement counterbalanced the loss in concrete strength. From R00 to R60, although confinement was significant, the loss in strength was more pronounced. In all CF cases, the peak capacity was typically reached due to the combined effect of steel yielding followed by concrete degradation.

For the purpose of assessing the comparative member ductility, the ultimate displacement δ_u was assumed as corresponding to a 15% reduction in the peak moment. As shown in Table 5, the yield, peak, and ultimate displacements generally decreased with higher axial loads. For the ultimate displacements, the R30 specimens had larger values compared to R00 (9.3% higher on average), while the R60 specimens had similar ultimate displacements compared with R00. Although an increase in rubber content increases the ductility of concrete materials, a significant reduction in the strength of the infill concrete may have some detrimental effects on the restraint provided to the local stability of the steel tube. This may explain the slightly higher ductility observed for R30 specimens compared to the R60 counterparts.

Table 5 also gives the values of the ductility index μ, considered herein as:

$$\mu = \frac{\delta_u}{\delta_y} \tag{4}$$

This index can also be used for assessing the member ductility in terms of the ratio between the ultimate and yield displacements. It indicates broadly similar trends to δ_u, although these are affected by the variation in yield displacement. Overall, all the CF specimens had good ductility with μ larger than 6.0. As shown in Table 5, the drift ratios Δ_u of the CF specimens were 5.5%–9.2%, compared to 3.0%–4.6% for the hollow steel specimens, indicating a highly ductile response.

Table 5 also depicts the displacement at the onset of local buckling, $\delta_{buckle,DIC}$, estimated from the development of compressive strains obtained from DIC gauges crossing the buckling area (see Fig. 12), noting that a further detailed assessment of this effect is given in Section 4.4. The derived displacements were cross-checked against close visual observation of the continuous DIC images. In general, for the CF specimens, local buckling occurred broadly at a displacement of 50–70 mm, with $\delta_{buckle,DIC}$ decreasing with the increase in axial load. For all members, local buckling occurred well into the inelastic range after the peak capacity was reached. Compared with ST members, local buckling in CF members occurred at significantly higher displacement levels leading to enhanced ductility.

Following local buckling, strain concentration and low cycle fatigue within the plastic hinge region typically lead to fracture of the steel tube in subsequent cycles. The displacement levels δ_{frac} at which fracture was observed in the tests are also given in Table 5. The fracture

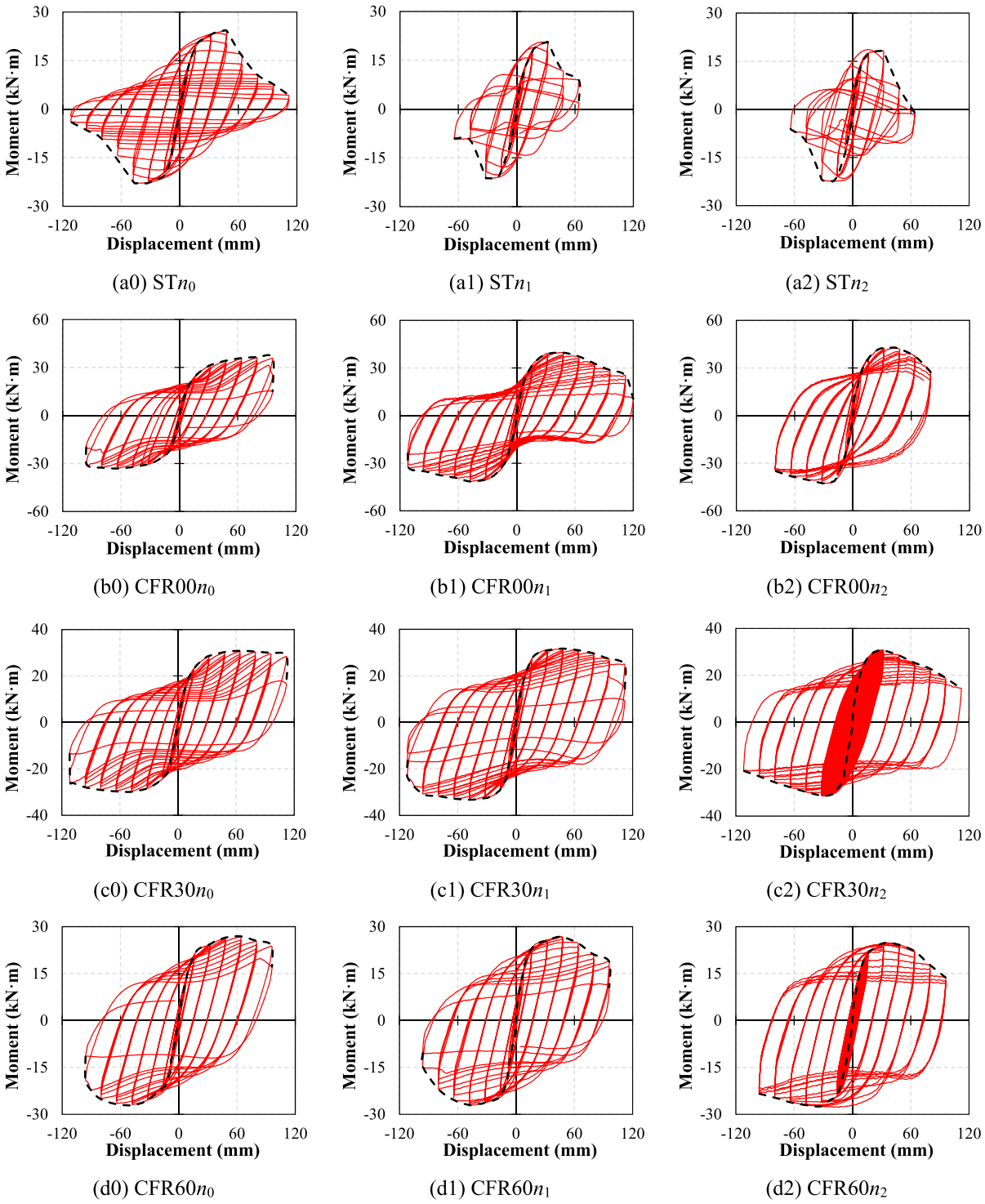

Fig. 5. Moment (M) versus displacement (δ_c) response.

displacements for all CF members were between 96 and 120 mm, noting that for the CFn_0 specimens δ_{frac} was similar to δ_u as no notable degradation occurred in the response. Based on the test data, the fracture occurred at a displacement typically larger than 1.5 times the displacement corresponding to local buckling.

Based on discussions presented above in this section, analytical assessments and comparisons are carried out below in the following section in order to enable prediction of the key response parameters.

4. Analytical assessments

4.1. Member stiffness

Simple analytical approaches for predicting the member stiffness are considered herein, and their results are compared with the experimental stiffness k_{test} reported in Section 3.2 above. For a cantilever member, the theoretical stiffness is $3EI/L_c^3$, where EI is the sectional bending stiffness and L_c is the member length. Design procedures typically determine the sectional bending stiffness as:

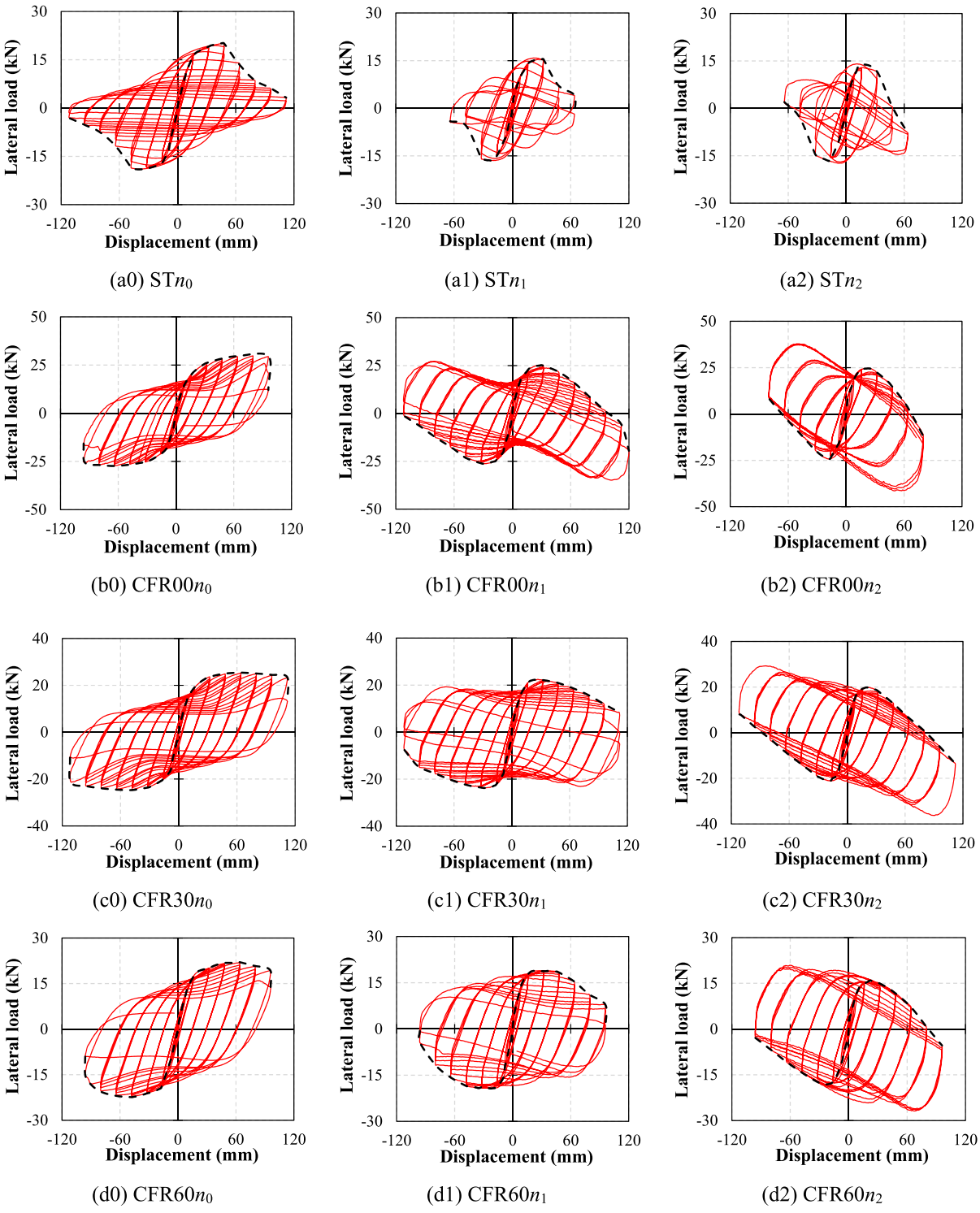

Fig. 6. Lateral load (V_H) versus displacement (δ_c) response.

$$EI = E_s I_s + \beta_c E_c I_c \tag{5}$$

where E_s and E_c are the elastic moduli for steel and concrete, respectively, while I_s and I_c are the second area moments for the steel and concrete sections, respectively, whilst β_c is a reduction factor considering concrete cracking which differs depending on the code. The value of β_c is 1.0 in BS5400 [36], 0.8 in AISC [37], 0.6 in Eurocode 4 [38], and 0.2 in AIJ [39] and ACI 318 [40]. Based on previous material tests on RuC [31], it was found that these codified E_c expressions for normal concrete cannot be used for RuC. Instead, for RuC, the following expression is adopted herein [31]:

$$E_{rc} = 12000\left(\frac{f_{rc}}{10}\right)^{\frac{2}{3}} \tag{6}$$

while for normal concrete, the Eurocode 4 [38] expression is adopted:

$$E_c = 22000\left(\frac{f_c}{10}\right)^{0.3} \tag{7}$$

The member stiffness obtained based on Eq. (5) above is shown in

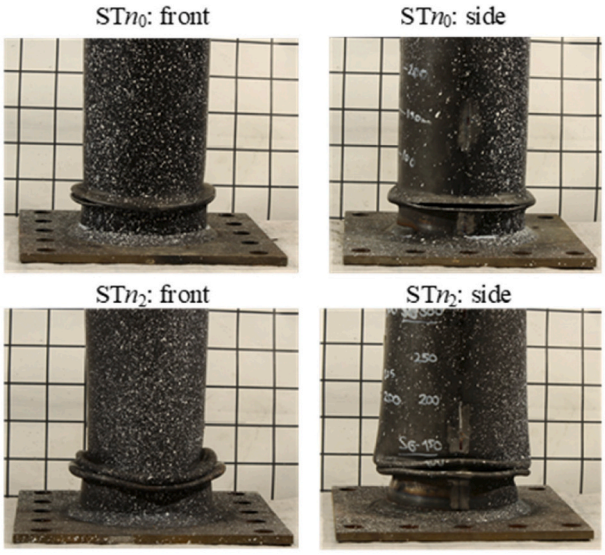

Fig. 7. Local buckling and fracture of the ST specimens at final states.

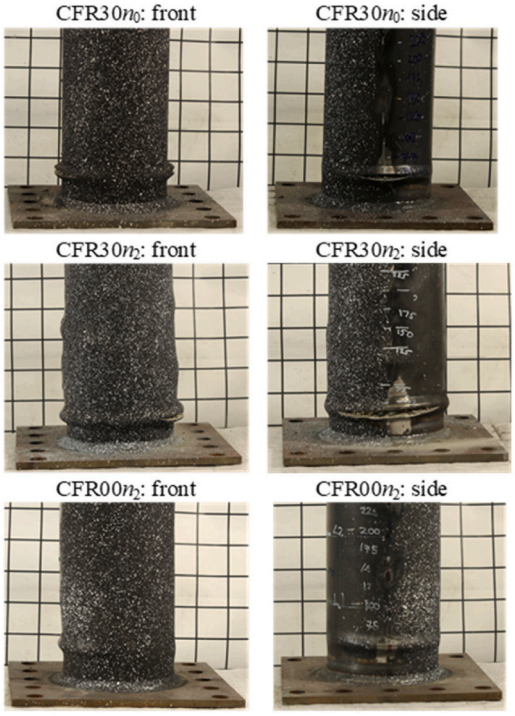

Fig. 8. Local buckling and fracture of the CF specimens at final states.

Table 6. It is found that a β_c value of 0.6, as suggested by Eurocode 4 [38], provides a close prediction, within less than 10% compared to the test results for specimens without axial loading. However, this difference increases for members subjected to axial loading as its influence is not captured within the above expressions. Accordingly, based on the test results, the following equations are proposed for considering the axial load ratio v_a to obtain a modified member stiffness (k_p):

$$k_p = k_{EC4}\left(1 + 0.15v_a^{0.3}\right) \text{ for normal concrete} \tag{8}$$

$$k_p = k_{EC4}\left(1 + 0.40v_a^{0.3}\right) \text{ for rubberised concrete} \tag{9}$$

In this study, n_0, n_1, n_2 refer to nominal axial load ratios v_a of 0.0, 0.15, 0.3, respectively. The proposed equations offer a better prediction with an average of 0.99 and a standard deviation of 0.06, compared to the Eurocode 4 predictions, which give an average of 1.13 and a standard deviation of 0.13. Hence Eqs. (8) and (9) provide a more reliable prediction, within the test data ranges considered herein.

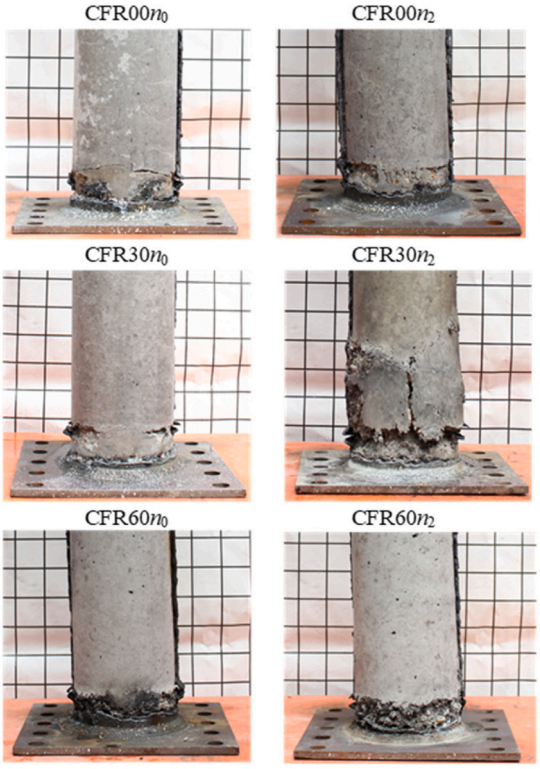

Fig. 9. Infill concrete inside the CF specimens at final states.

4.2. Strength interaction

4.2.1. Design approaches

Bending-axial (*M-N*) strength interaction representations are typically used for design. In Eurocode 4 [38,41], the strength interaction of composite sections is based on ideal plasticity. This assumes that at peak capacity, the constituent materials all reach their maximum strength and have perfectly plastic behaviour. For steel, the yield strength is maintained in both compression and tension whereas, for concrete, the compressive strength f_c is reached while tensile strength is ignored. Based on these assumptions, four characteristic points A, B, C, D on the *M-N* interaction curve, illustrated in Fig. 13, could be evaluated as follows:

$$N_{pl,R} = \eta_s f_s A_s + \left(1 + \eta_c \frac{t}{D}\frac{f_s}{f_c}\right) f_c A_c \tag{10}$$

$$N_{pm,R} = f_c A_c \tag{11}$$

$$M_{max,R} = f_s W_{ps} + \frac{f_c W_{pc}}{2} \tag{12}$$

$$M_{pl,R} = f_s\left(W_{ps} - W_{ps,n}\right) + \frac{f_c\left(W_{pc} - W_{pc,n}\right)}{2} \tag{13}$$

where $N_{pl,R}$ is the pure axial compression capacity (Point A); $N_{pm,R}$ is the compression capacity at Point B corresponding to the neutral axis location B—B in Fig. 13; $M_{max,R}$ is the maximum moment at Point D corresponding to neutral axis location D-D; $M_{pl,R}$ is the pure bending moment at Point B and C (B—B and C—C); η_s and η_c are factors for steel

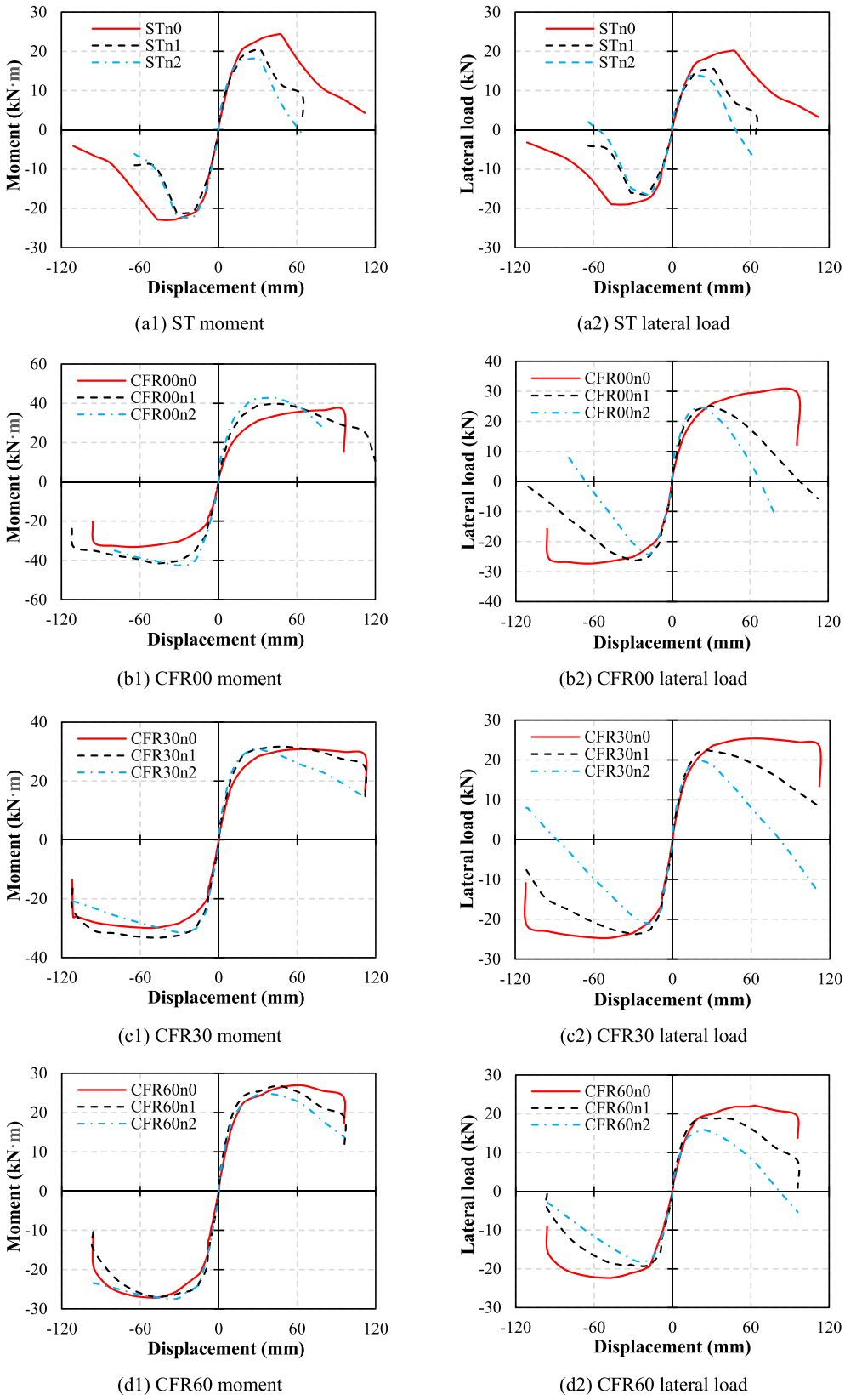

Fig. 10. Comparisons of envelope responses for different axial load levels.

and concrete considering the confinement effect in pure axial compression, with $\eta_s = 0.25(3 + 2\lambda)$ and $\eta_c = 4.9–18.5\,\lambda + 17\lambda^2$, where λ is the nondimensional relative slenderness [38]; A_c is the area of concrete; W_{ps} and W_{pc} are the plastic section moduli for the whole cross-sections of the steel tube and concrete core, respectively; $W_{ps,n}$ and $W_{pc,n}$ are the plastic section moduli for the steel tube and the concrete core within Region 2 in Fig. 13; h_n is the distance between characteristic axes in Fig. 13. By connecting the four points, a tri-linear *M-N* curve

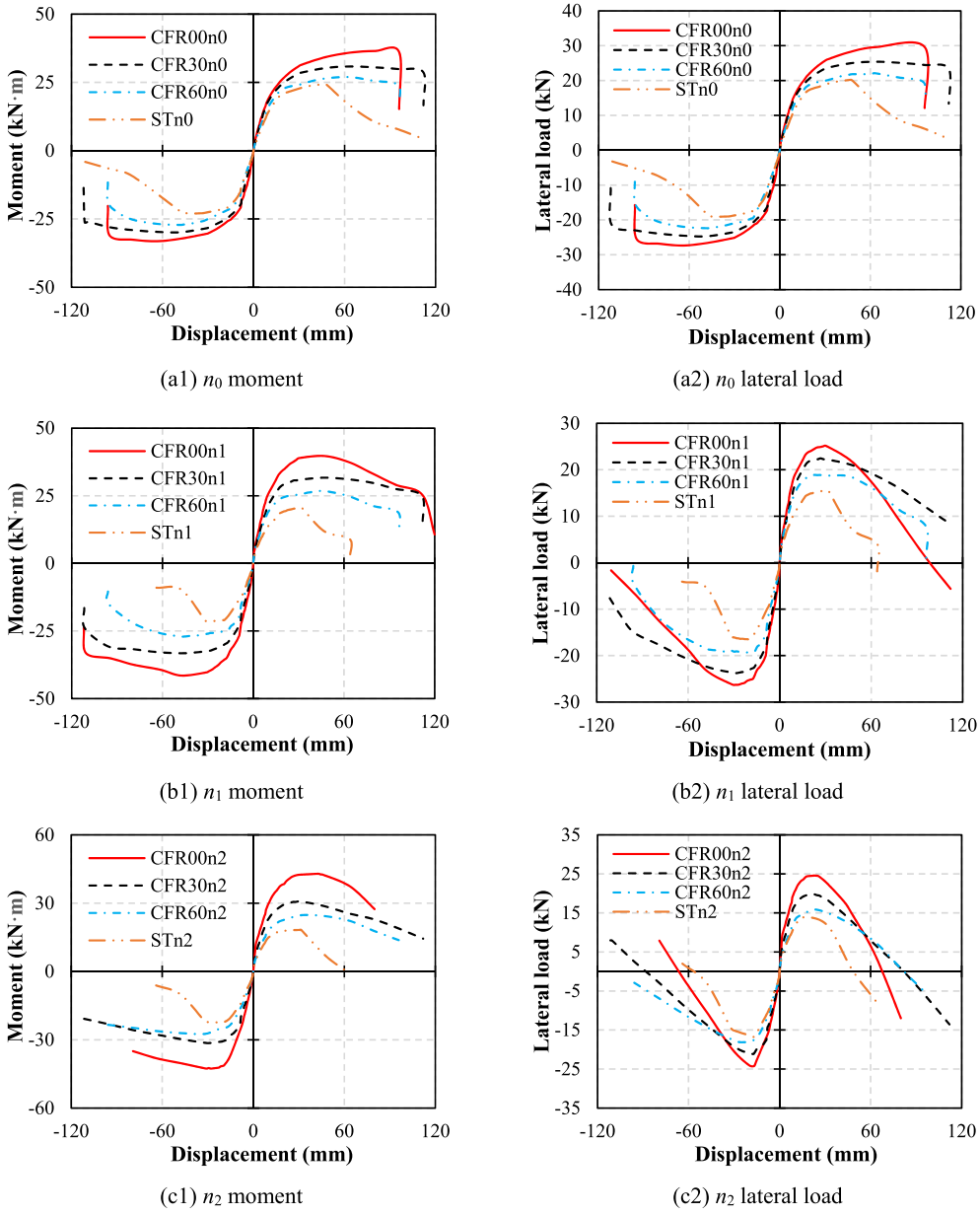

Fig. 11. Comparisons of envelope responses for different configurations.

Table 5
Characteristic parameters for all the cyclic test specimens.

ID	f_{rc} (MPa)	N (kN)	k_{test} (kN/mm)	M_y (kN·m)	M_{peak} (kN·m)	V_y (kN)	V_{peak} (kN)	δ_y (mm)	δ_{Vpeak} (mm)	δ_{Mpeak} (mm)	$\delta_{buckle,DIC}$ (mm)	δ_u (mm)	$\triangle_u$ (%)	δ_{frac} (mm)	μ
STn_0	–	4.8	1.34	19.0	23.6	15.8	19.6	14.7	42.7	42.7	43.7	54.9	4.6	112	3.74
STn_1	–	66.8	1.44	14.8	21.0	11.7	16.0	11.1	26.6	29.0	29.4	36.6	3.1	64	3.30
STn_2	–	134.8	1.64	14.7	20.3	11.3	15.3	9.5	15.9	25.3	22.2	35.6	3.0	–	3.74
CFR00n_0	81.4	7.1	2.10	23.8	34.8	19.7	28.5	13.9	71.7	71.7	63.6	95.5	8.0	96	6.88
CFR00n_1	81.4	288.4	2.38	27.5	40.6	20.3	25.7	10.8	29.8	47.3	52.2	85.1	7.1	120	7.87
CFR00n_2	81.4	592.9	2.56	28.3	42.7	18.9	24.3	9.6	20.3	35.6	48.8	69.1	5.8	–	7.20
CFR30n_0	18.9	6.4	1.82	22.3	30.3	18.5	25.0	13.8	56.0	56.0	59.0	110.5	9.2	112	8.00
CFR30n_1	18.9	136.9	2.10	23.6	32.5	18.4	23.1	11.0	27.6	46.3	53.3	99.9	8.3	112	9.09
CFR30n_2	18.9	277.9	2.27	22.6	31.1	16.7	20.5	9.1	19.1	30.3	50.9	65.6	5.5	112	7.23
CFR60n_0	6.6	8.0	1.47	20.6	27.1	17.2	22.2	15.2	55.6	55.6	69.8	91.4	7.6	96	6.03
CFR60n_1	6.6	102.5	1.80	20.2	26.9	15.9	19.1	10.7	24.4	47.4	54.1	73.6	6.1	96	6.87
CFR60n_2	6.6	211.7	1.69	18.1	26.1	13.3	17.0	10.2	24.3	32.2	51.0	81.8	6.8	96	8.05

Note: the parameters were calculated as the average of the positive branch and negative branch.

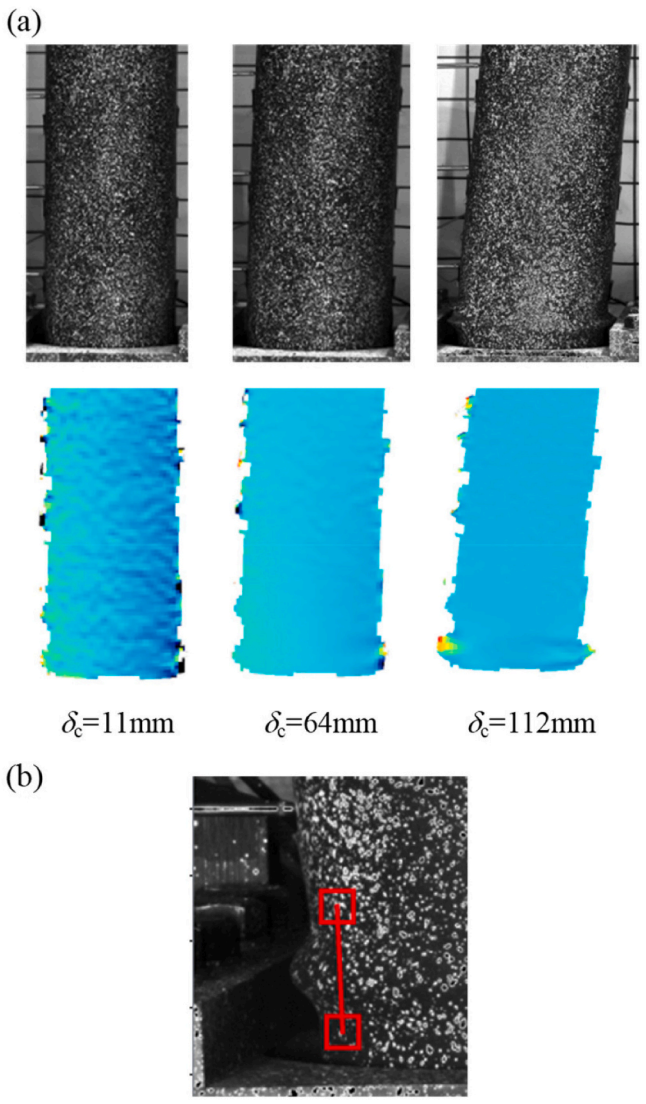

Fig. 12. Typical DIC axial strain results: (a) plots at different displacements; (b) virtual gauge crossing the buckling area.

could be derived as shown in Fig. 13.

The resulting interaction curves for the three different CF cross-sections used in the tests are depicted in Fig. 14 together with the test results. Note that in Eqs. (10)–(13) only $N_{pl,R}$ accounts for confinement, hence at Point A this effect is fully considered. In contrast, for Branch A-C, the confinement effect is partially considered, and is totally disregarded for Branch C-D-B of the interaction curve. The assumption of considering confinement effects only under significant axial loading is typically in agreement with the results of composite members incorporating normal concrete materials [42,43]. As noted above, the Eurocode 4 approach involves several idealisations and limitations [38,41], including those related to full plastic stress distribution and simplified consideration of confinement. Additionally, the code design expressions were validated on a database which does not cover material strength ranges for rubberised concrete.

4.2.2. Sectional analysis

To estimate the adequacy of the codified design expressions, the strength interaction curve for the configurations investigated in this paper was also estimated analytically through fibre-based section analysis incorporating characteristic uniaxial stress-strain responses for steel and concrete. The general form of the widely-used concrete confinement model proposed by Mander et al. [44] was employed. According to the model, the increased strain at critical state ε_{cc1} could be assumed as:

$$\varepsilon_{cc1} = \varepsilon_{c1}\left[1 + 5\left(\frac{f_{cc}}{f_c} - 1\right)\right] \tag{14}$$

where ε_{c1} is the critical strain of the unconfined concrete, based on Eurocode 2 [45] for normal concrete, and using the approach suggested by Bompa et al. [31] for rubberised concrete; f_c is the unconfined strength based on the material tests; f_{cc} is the confined concrete strength, which was considered based on the confinement factor from Eurocode 4 [38] as in Eq. (10). For rubberised concrete, a modification factor was considered based on previous studies on axially-loaded RuCFST members [22] as follows:

$$\lambda_{rcc} = 1 - 0.4\rho_{vr} \tag{15}$$

$$\frac{f_{cc}}{f_c} = \lambda_{rcc}\left(1 + \eta_c \frac{t}{D}\frac{f_s}{f_c}\right) \tag{16}$$

4.2.3. Modified expressions

The *M-N* strength interactions presented in Fig. 14 compare the curves from the Eurocode 4 approach [38,41] and the sectional analysis described above, against the test results obtained in this study. The results from the sectional analysis without steel hardening are shown since it had an insignificant influence on the member capacity. As shown in Fig. 14, for normal concrete, Eurocode 4 and sectional analysis provides similar results, and the predictions are conservative with respect to the test results. For rubberised concrete, the sectional analysis gives similar results as Eurocode 4 for bending, but provide lower compression capacity predictions for axial-loaded cases, which deviate proportionally from the code with the increase in rubber contents. For both the normal and rubberised concrete infilled members, the predicted capacities are notably more conservative than the test results in the bending region, particularly when compared with monotonic test results [22]. These differences become larger with the increase in rubber content. Although

Table 6
Stiffness characteristics.

ID	f_c, f_{rc} (MPa)	E_c, E_{rc} (MPa)	EI (MN·m^2)	k_{test} (kN/mm)	k_{EC4} (kN/mm)	k_{test}/k_{EC4}	k_p (kN/mm)	k_{test}/k_p
CFR00n_0	81.4	41,268	1.29	2.10	2.24	0.94	2.24	0.94
CFR00n_1	81.4	41,268	1.29	2.38	2.24	1.06	2.43	0.98
CFR00n_2	81.4	41,268	1.29	2.56	2.24	1.14	2.47	1.04
CFR30n_0	18.9	18,348	0.98	1.82	1.70	1.07	1.70	1.07
CFR30n_1	18.9	18,348	0.98	2.10	1.70	1.24	2.08	1.01
CFR30n_2	18.9	18,348	0.98	2.27	1.70	1.34	2.17	1.04
CFR60n_0	6.6	9095	0.85	1.47	1.48	0.99	1.48	0.99
CFR60n_1	6.6	9095	0.85	1.80	1.48	1.22	1.82	0.99
CFR60n_2	6.6	9095	0.85	1.69	1.48	1.14	1.89	0.90
					AVE.	1.13	AVE.	0.99
					STD.	0.13	STD.	0.06

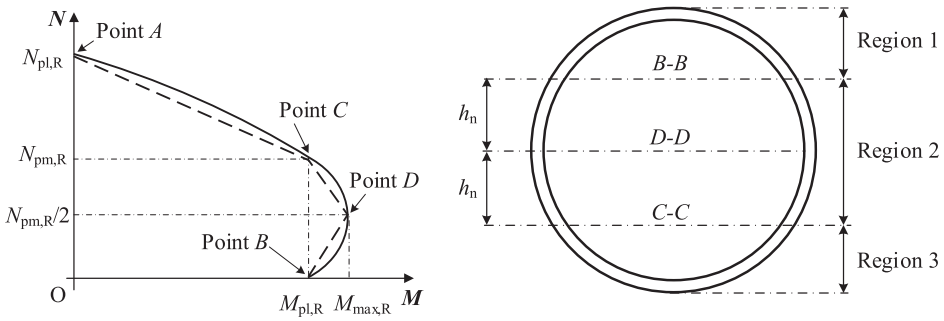

Fig. 13. M-N interaction prediction based on Eurocode 4.

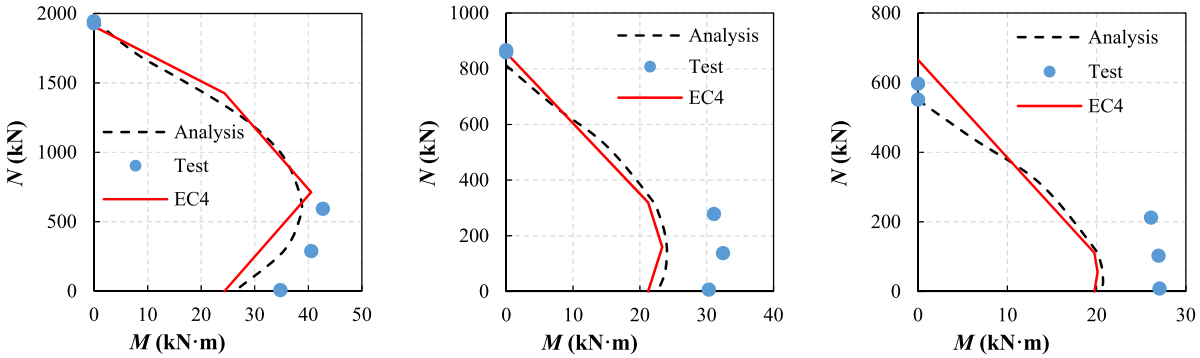

Fig. 14. Bending-axial interaction curves for CF members.

hardening has an insignificant influence in the case of monotonic loading, its effect becomes more pronounced under repeated cyclic loading. The increase in rubber content also has a positive influence on cyclic hardening as it enhances confinement and decreases concrete degradation.

Considering these differences between predictions and tests, Eqs. (10)–(13) are modified using rubber content dependent factors as follows, where λ_{rcc} is adopted for the axial loading and γ_{rcc} for the bending region.

$$N_{pl,R\_RuC} = \eta_s f_s A_s + \lambda_{rcc}\left(1+\eta_c \frac{t}{D}\frac{f_s}{f_c}\right) f_c A_c \tag{17}$$

$$M_{max,R\_RuC} = \gamma_{rcc} M_{max,R} \tag{18}$$

$$M_{pl,R\_RuC} = \gamma_{rcc} M_{pl,R} \tag{19}$$

$$\gamma_{rcc} = 1 + 0.3\rho_{vr}^{0.3} \tag{20}$$

The above equations expand the bending region of the M-N curve and reduce the pure axial capacity for the rubberised concrete case, yet reverts to the normal concrete case if ρvr = 0. The results of the proposed method compared with the Eurocode 4 predictions are shown in Fig. 15. It is evident that by applying the proposed modifications, Eqs. (17)–(20) offer significantly improved predictions for both the bending and compression capacities of RuCFST cases. Note that γrcc is a factor accounting for cyclic hardening, which can be conservatively assumed as unity in design.

4.3. Plastic hinge length

The extent of the plastic hinge is important in evaluating the ductility of members as well as for detailing purposes. To this end, the DIC data

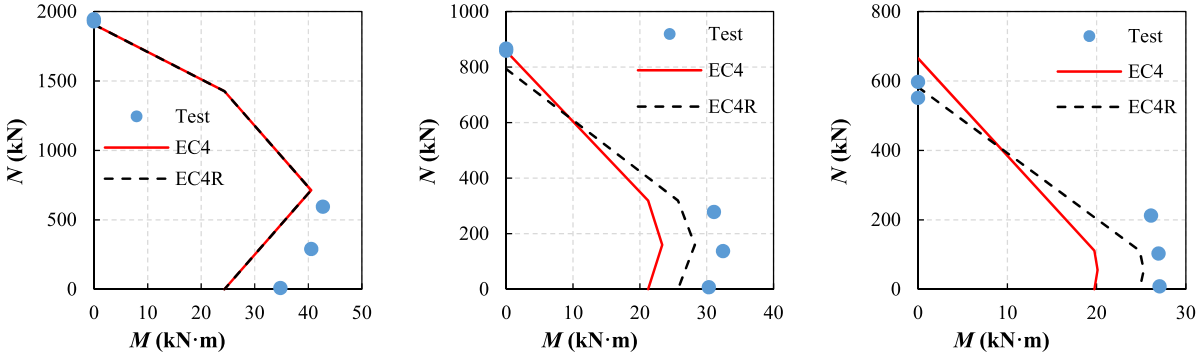

Fig. 15. Modified bending-axial interaction curves for CF members.

was used to assess the plastic hinge length (L_{p_test}) from the experimental results. The strain gauge measurements, which only covered specific locations in the test specimens, were used for checking the consistency of the information at these positions.

The plastic hinge length L_{p_cal} for a cantilever member can also be estimated theoretically [46], as follows:

$$L_{p\_cal} = \left(1 - \frac{M_y}{M_{peak}}\right) L_c \tag{21}$$

Based on the DIC data, the strain distributions at both sides around the fixed end of typical CF members are illustrated in Fig. 16, from the start of loading up to the peak moment. The legend indicates corresponding displacement levels in mm. Only typical strain distribution patterns are shown for brevity since others are similar. The plastic hinge lengths obtained from the test data at the peak moment (average yield region length of both sides) are summarized in Table 7, together with the predictions from Eq. (21) above. The comparison indicates that Eq. (21), alongside the definition of yield and ultimate moments adopted in this study, provides a close estimate of the plastic hinge length. Note that the plastic hinge length typically increases slightly with the level of co-existing axial loading, but the values were largely within the range of 2.0–2.5D. For simplicity, an overall average value of 2.25D could be reasonably adopted as indicated in Table 7.

Table 7
Plastic hinge length.

ID	M_y (kN·m)	M_{peak} (kN·m)	L_{p_test} (mm)	L_{p_cal} (mm)	L_{p_test}/L_{p_cal}	$L_{p\_test}/2.25D$
CFR00n_0	23.8	34.8	329	380	0.87	0.96
CFR00n_1	27.5	40.6	408	386	1.06	1.19
CFR00n_2	28.3	42.7	324	406	0.80	0.95
CFR30n_0	22.3	30.3	299	317	0.94	0.87
CFR30n_1	23.6	32.5	322	328	0.98	0.94
CFR30n_2	22.6	31.1	339	329	1.03	0.99
CFR60n_0	20.6	27.1	309	287	1.08	0.90
CFR60n_1	20.2	26.9	325	302	1.08	0.95
CFR60n_2	18.1	26.1	401	370	1.08	1.17
				AVE.	0.99	0.99
				STD.	0.10	0.11

4.4. Ultimate criteria

As discussed in Section 3.2 above, local tube buckling occurred in the cyclic tests at large lateral deformations and was typically followed by fracture due to low cycle fatigue. This section examines simple analytical approaches for predicting the onset of local buckling. Available expressions for estimating the critical inelastic buckling strain for CFST sections are firstly reviewed and compared with the results obtained from the tests. The sectional analysis discussed in Section 4.2 above is also used in the comparative assessment and for developing a simplified approach for predicting the displacement corresponding to the onset of local buckling.

4.4.1. Critical strains

The critical strain, corresponding to the onset of local buckling, can be assessed using Eqs. (22)–(23), by adapting the theoretical buckling stress relationships as reported in previous studies [35]. In the equations, ε_{cr} is the critical buckling strain, ε_y is the yield strain, f_s is the yield stress, and ν is Poison's ratio. For hollow steel circular tubes and CFST, the critical buckling strains ($\varepsilon_{cr,HS}$ and $\varepsilon_{cr,CFST}$, respectively) could be obtained from classical energy theory [47].

$$\varepsilon_{cr,HS} = \frac{2E_s}{\sqrt{3(1-\nu^2)}} \frac{t}{d} \frac{\varepsilon_y}{f_s} \tag{22}$$

$$\varepsilon_{cr,CFST} = \frac{2E_s}{\sqrt{(1-\nu^2)}} \frac{t}{d} \frac{\varepsilon_y}{f_s} \tag{23}$$

Eqs. (22)–(23) indicate that the critical buckling strain of CFST is $\sqrt{3}$ times that of the corresponding hollow steel section. For the specimens tested in this study, the above equations give buckling strains of 2.22% and 3.86% for the hollow steel and CF specimens, respectively. Based on the DIC strain data, the corresponding lateral displacements when the extreme fibre reached the critical buckling strain is shown in Table 8.

4.4.2. Drift levels

As discussed in Section 4.3, a linear curvature distribution can be assumed along the plastic hinge length of 2.25D from the fixed end, whilst the curvature above this region is comparatively small and can be neglected. Based on these assumptions, the lateral drift Δ of the cantilever beam could be calculated as a function of the fixed end curvature φ. Using Eq. (24) and assuming ideal plasticity for both steel and concrete (with confined f_{cc} from Eq. (16)), the drift corresponding to local buckling could be theoretically derived. As shown in Fig. 17, the equilibrium condition in the cross-section is given by Eq. (25), in which N is the axial force considering compression as positive, and H_n is the neutral axis depth (distance from bottom fibre) which can be evaluated using Eq. (26).

Based on the critical buckling strain ε_{cr} (Eq. (27)), the drift could be estimated from Eq. (28). Accordingly, the drifts Δ_{CFST} or Δ_{HS} can be determined from Eqs. (29) and (30), respectively. Note that, for a hollow steel tube, Eq. (30) was derived by considering $f_{cc} = 0$ and dividing by $\sqrt{3}$.

$$\Delta(\varphi) = \frac{\varphi}{2} 2.25D = 1.125D{\cdot}\varphi \tag{24}$$

$$N = f_{cc}\left(\frac{D}{2}-t\right)^2 arccos\left(\frac{H_n - \frac{D}{2}}{\frac{D}{2}}\right) - f_s Dt\left[\pi - 2arccos\left(\frac{H_n - \frac{D}{2}}{\frac{D}{2}}\right)\right] \tag{25}$$

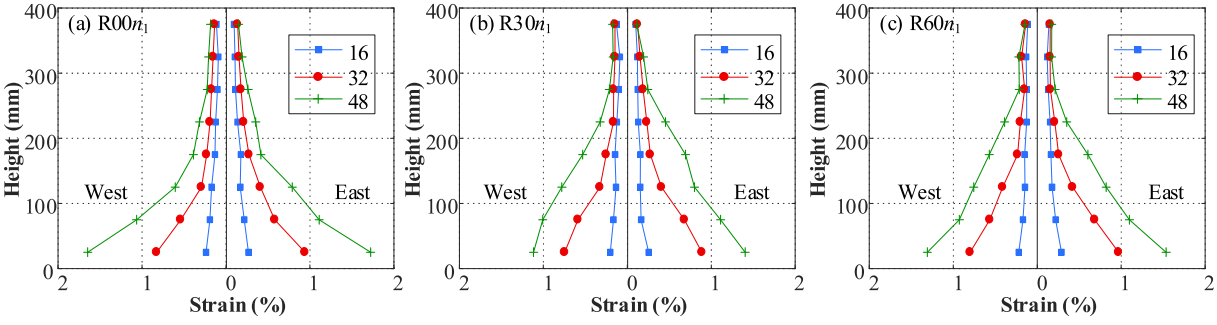

Fig. 16. Typical strain distributions at fixed end based on DIC data (legends: displacement levels in mm).

Table 8
Displacement corresponding to local buckling initiation.

ID	f_{rc} (MPa)	N (kN)	$\delta_{buckle,DI}$ (mm)	$\delta_{buckle,A}$ (mm)	$\delta_{buckle,T}$ (mm)	$\delta_{buckle,TD}$ (mm)	$\delta_{buckle,TP}$ (mm)	Comparison	
								TD/A	TP/DIC
STn$_0$	–	4.8	43.7	53	59	–	–	–	–
STn$_1$	–	66.8	29.4	43	48	–	–	–	–
STn$_2$	–	134.8	22.2	37	40	–	–	–	–
CFR00n$_0$	81.4	7.1	63.6	180	746	166	62	0.92	0.97
CFR00n$_1$	81.4	288.4	52.2	101	270	98	51	0.97	0.97
CFR00n$_2$	81.4	592.9	48.8	70	139	70	47	0.99	0.96
CFR30n$_0$	18.9	6.4	59.0	120	230	123	62	1.03	1.05
CFR30n$_1$	18.9	136.9	53.3	86	139	89	53	1.04	1.00
CFR30n$_2$	18.9	277.9	50.9	66	95	71	49	1.08	0.97
CFR60n$_0$	6.6	8.0	69.8	108	164	98	63	0.91	0.90
CFR60n$_1$	6.6	102.5	54.1	84	115	80	54	0.95	1.00
CFR60n$_2$	6.6	211.7	51.0	66	85	68	48	1.03	0.95
						AVE.		0.99	0.97
						STD.		0.06	0.04

Note: all buckling displacements are based on critical buckling strain, with subscript DIC—DIC strain, A = sectional analysis, T = theoretical analysis, TD = theoretical analysis considering modification for concrete degradation, TP = proposed theoretical method considering both concrete degradation and cyclic loading.

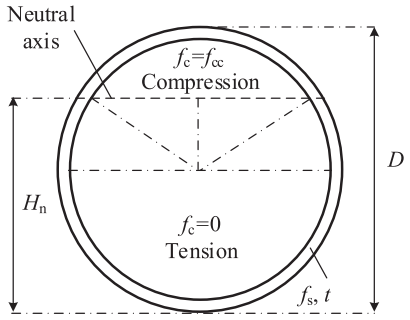

Fig. 17. Section analysis on neutral axis.

$$H_n = \frac{D}{2}\left\{1 + cos\left[\frac{N + f_s Dt\pi}{f_{cc}\left(\frac{D}{2}-t\right)^2 + 2f_s Dt}\right]\right\} \tag{26}$$

$$\varepsilon_{cr} = \varphi(D - H_n) \tag{27}$$

$$\Delta = 1.125D{\cdot}\varphi = 1.125\frac{D\varepsilon_{cr}}{D - H_n} \tag{28}$$

$$\Delta_{CFST} = \frac{t}{D\sqrt{(1-\nu^2)}}\cdot\frac{2.25}{1 - \frac{1}{2}\left\{1 + cos\left[\frac{N + f_s Dt\pi}{\lambda_{rcc}\left(1+\eta_c\frac{t}{D}\frac{f_s}{f_c}\right)f_c\left(\frac{D}{2}-t\right)^2 + 2f_s Dt}\right]\right\}} \tag{29}$$

$$\Delta_{HS} = \frac{t}{D\sqrt{3(1-\nu^2)}}\cdot\frac{2.25}{1 - \frac{1}{2}\left[1 + cos\left(\frac{N + f_s Dt\pi}{2f_s Dt}\right)\right]} \tag{30}$$

Using Eq. (24), while considering concrete degradation and steel hardening, the buckling displacements based on monotonic section analysis are shown in Table 8 and denoted as $\delta_{buckle,\ A}$. Evidently, the monotonic buckling displacement is significantly larger than the cyclic counterpart, as expected, due to the significant strain accumulation that occurs under repeated cyclic loading. In the sectional analysis, CFR30 and CFR60 also have similar buckling displacement values as they have comparable confined strengths based on Eq. (16). Moreover, CFR00n_0 has a larger buckling displacement since it has a higher concrete strength and neutral axis position. However, when the axial load increases, CFR00n_1 and CFR00n_2 exhibit similar buckling displacements as for CFR30 and CFR60 since the neutral axis locations are comparable for the same axial load levels.

The predicted buckling displacements using Eqs. (29) and (30) are given in Table 8. It is shown that the buckling displacement decreases with the increase in axial load or concrete strength. Similar trends are observed between the theoretical results and sectional analyses. For CFST, the theoretical values are larger than the analytical predictions mainly due to the disregard of concrete strength post-peak degradation. This difference reduces with the increase in axial loads and decrease in concrete strength. For the purpose of this assessment, an empirical reduction factor ξ_D could be considered based on these trends in order to modify the theoretical results for consistency with sectional analyses, as follows:

$$\Delta_{CFST,D} = \xi_D \Delta_{CFST} \tag{31}$$

$$\xi_D = 0.65 - 0.005f_{rc} + (0.0035f_{rc} + 0.64)v_a \tag{32}$$

Furthermore, to consider the difference between monotonic and cyclic loading histories, another reduction factor χ_C is also proposed as follows:

$$\Delta_{CFST,P} = \chi_C \xi_D \Delta_{CFST} \tag{33}$$

$$\chi_C = (0.45 - 1.25v)\rho_{vr} + v_a + 0.37 \geq v_a + 0.37 \tag{34}$$

The modified theoretical results for CFST, adjusted using the proposed reduction factors to account for the influence of concrete degradation and cyclic loading, are shown in Table 8, and denoted as $\delta_{buckle,\ TD}$, and $\delta_{buckle,\ TP}$, respectively. Comparing the results from Eq. (31) and the sectional analysis (both monotonic), the average ratio is 0.99 with a standard deviation of 0.06; comparing the results from Eq. (33) and the test results (both considered as cyclic), the average ratio is 0.97 with a standard deviation 0.04. The comparisons indicate that the proposed equations can be adopted to provide a reasonable and conservative prediction of the buckling displacements for the test specimens. Nonetheless, it clearly needs to be further validated and calibrated against a larger database of experimental results supported by detailed monotonic and cyclic numerical parametric assessments.

4.5. Energy dissipation

To evaluate the energy dissipation from the cyclic test results, the area of each loop at different displacement levels was calculated based on the lateral load versus displacement (V_H-δ_c) responses shown in Fig. 6. The energy determined based on V_H-δ_C response is equivalent to that dissipated by the specimen. Fig. 18 depicts the energy of the first and third loops at different displacement levels for different specimens, up to relevant drift levels of about 5%. To permit meaningful nondimensional comparisons, the energy is normalized by the plastic moment capacity of the cross-section. The first and third loop results are shown in

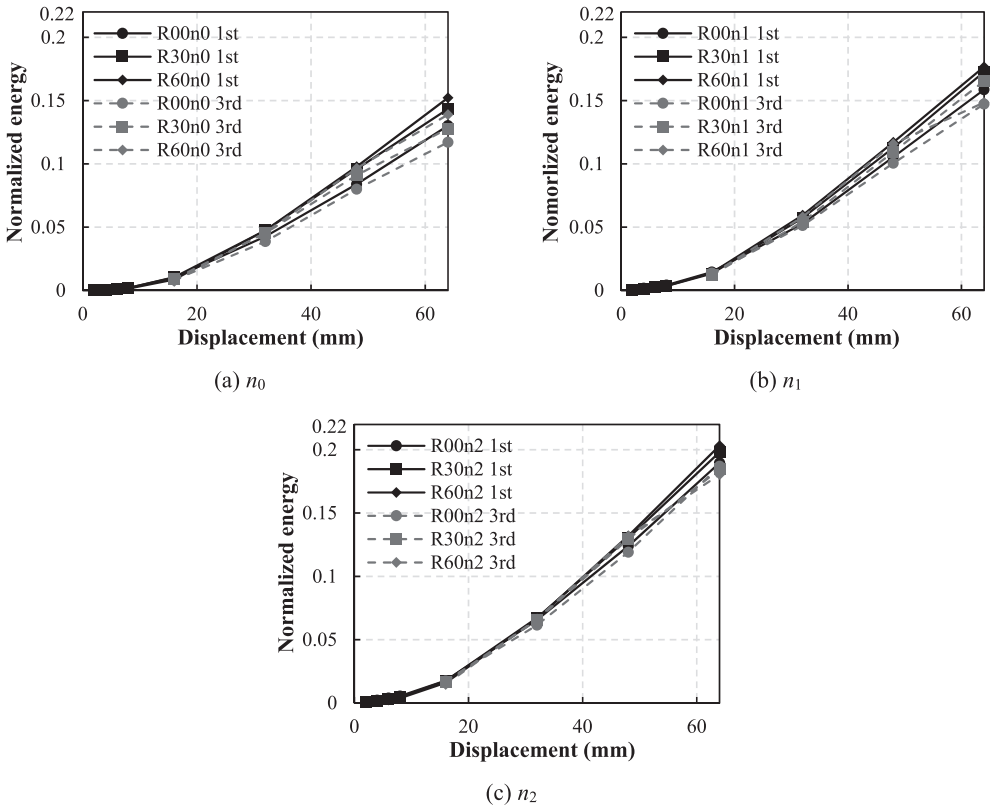

Fig. 18. Comparisons of normalized energy dissipation for members with different infill materials.

solid and dashed lines, respectively. The average cyclic energy degradation values are also summarized in Table 9.

As shown in Fig. 18, the normalized energy dissipation increased with the rubber ratio for all axial load levels. The influence of the rubber ratio on the normalized energy dissipation decreased with the increase in the axial load level. At a drift of 5.3%, for n_0 axial load, the normalized energy of R30 was 10.2% higher than R00 while R60 was 16.9% higher than R00; these values were respectively 8.8% and 11.3% for n_1 cases; and 4.5% and 7.2% for n_2 cases.

Fig. 18 and Table 9 also indicate that with the increase in axial load the energy dissipation increased while the cyclic degradation decreased. With the range of rubberised concrete-filled tube specimens tested herein, this increase in energy dissipation is attributed to the more pronounced enhancement in confinement with higher axial loads compared to the corresponding increase in capacity. It should also be noted from the results in Table 9 that, in all cases, the cyclic degradation at different load levels was broadly similar and relatively modest for the type of members considered in this study. Overall, within the experimental ranges examined in this study, it is shown that the partial rubber replacement of mineral aggregates in the concrete infill of circular steel tubes provides generally favourable performance in terms of ductility and energy dissipation capabilities.

Table 9
Cyclic degradation of CF members.

Axial load	Cycle number	AVE.			STD.		
		R00	R30	R60	R00	R30	R60
n_0	2nd	0.91	0.94	0.95	0.03	0.04	0.05
	3rd	0.88	0.89	0.92	0.04	0.04	0.06
n_1	2nd	0.95	0.96	0.95	0.02	0.02	0.04
	3rd	0.92	0.93	0.91	0.04	0.03	0.07
n_2	2nd	0.98	0.96	0.96	0.03	0.03	0.04
	3rd	0.98	0.93	0.93	0.03	0.05	0.07

Finally, as mentioned before, it is important to note that this experimental study focused on assessing the inelastic lateral cyclic behaviour of circular steel tubes filled with normal and rubberised concrete, and under co-existing axial loads representing typical gravity conditions under seismic situations. The response of infilled tubes with different cross-section configurations, or those involving elastic local or global instabilities are beyond the scope of this study.

5. Concluding remarks

This paper investigated the structural behaviour of rubberised concrete filled steel tubes (RuCFST) under lateral cyclic displacements and co-existing axial loading. The rubber replacement ratio was varied up to 60%, under axial loads reaching up to 30% of the nominal cross-section capacity. The experimental results were discussed in detail and provided significant insights into the main behavioural characteristics. Analytical treatments were also carried out in order to propose simplified relationships for predicting the stiffness, moment-axial strength interaction, plastic hinge length, and local ductility criteria of the composite members considered. Additional specific observations and conclusions are highlighted below.

1. In addition to the complementary material and section characterization tests, a total of 12 cyclic member tests were carried out, including 9 concrete-infilled and 3 hollow-steel specimens. Three axial load levels (0%, 15% and 30% of the axial cross-section capacity) and three rubber ratios (0%, 30% and 60%) were considered. The ultimate behaviour was typically characterised by concrete degradation, local buckling, and steel fracture within the plastic hinge region.
2. The use of high rubber ratios led to a considerable loss in concrete strength of about 77% and 92% reduction, respectively, for R30 and R60 compared to R00. Nonetheless, the corresponding reduction in member capacity was much less significant due to the contribution of

the steel tube and the comparatively high confinement effects mobilised within the rubberised concrete. Compared to infilled members with R00, those incorporating R30 and R60 concrete had a reduction in moment capacity of approximately 20% and 30%, respectively, on average, for the various axial load levels considered.
3. In comparison with the members incorporating conventional concrete, the rubberised concrete members showed a hysteretic response with less pinching and exhibited up to about 10% and 17% increase in terms of the normalized ductility and energy dissipation, respectively, depending on the rubber content and the level of axial load.
4. Existing analytical approaches for predicting the member stiffness were shown to be adequate only for members with normal concrete and without axial load. Modified expressions were therefore proposed to account for the delayed cracking and enhanced confinement for rubberised concrete particularly in the presence of high axial load levels.
5. Analytical and design procedures were found to underestimate the cyclic bending capacities of the infilled members, particularly those incorporating rubberised concrete. This is attributed to the influence of cyclic hardening in steel and the considerable concrete confinement effects in the infill rubberised concrete, which are not adequately captured. To account for this, a rubber content dependent factor was proposed to modify the moment capacity in the design procedure adopted in Eurocode 4. In contrast, it was shown that Eurocode 4 overestimates the axial capacity of rubberised concrete filled tubular members, hence necessitating the use of a rubber content dependent reduction factor to enable a safe prediction.
6. Detailed assessment of the experimental data showed that although the estimated plastic hinge length was slightly influenced by the level of axial load, it was typically within the range 2.0–2.5 times the cross-section diameter of the member in all the infilled members. It was also shown that predictions based on the estimated yield and peak moments can be used to obtain reasonably good predictions of the plastic hinge length.
7. The test results provided direct experimental information on the strain and deformation levels corresponding to the onset of inelastic local buckling in the concrete filled tubular members. Theoretical estimates, in conjunction with monotonic section analysis, were then modified based on comparisons against the test results to provide simplified expressions for predicting the deformation levels corresponding to the initiation of inelastic local buckling. The cyclic test results also showed that subsequent fracture of the tube occurred typically at a displacement of at least 1.5 times that corresponding to the onset of local buckling.

Overall, the test results described in this paper demonstrate the favourable inelastic cyclic performance of circular steel tubes infilled with rubberised concrete and provided valuable data that can be used in future detailed numerical studies. The proposed prediction expressions for the key inelastic response parameters also provide the basis for developing practical assessment and design methods which are suitable for rubberised concrete-filled steel tubular members.

CRediT authorship contribution statement

A.Y. Elghazouli: Conceptualization, Formal analysis, Funding acquisition, Project administration, Resources, Supervision, Writing – original draft. **A. Mujdeci:** Data curation, Formal analysis, Investigation, Validation, Visualization, Writing – original draft. **D.V. Bompa:** Conceptualization, Methodology, Supervision, Validation, Writing – review & editing. **Y.T. Guo:** Data curation, Formal analysis, Investigation, Methodology, Software, Visualization, Supervision, Writing – original draft.

Declaration of Competing interest

The authors declare that they have no known competing financial interests or personal relationships that could have appeared to influence the work reported in this paper.

Data availability

Data will be made available on request.

Acknowledgments

The second author wishes to acknowledge the scholarship funding provided by the Turkish Ministry of National Education. The fourth author wishes to acknowledge the postdoc funding provided by Zijing Scholar Program of Tsinghua University, China. The authors would additionally like to thank the technical staff of the Structures Laboratories at Imperial College London, particularly Mr. T Stickland, for their assistance with the tests. The support of Adria Abruzzo, Breedon Group, Elkem and Sika through material provision is also gratefully acknowledged.

References

[1] M. Sienkiewicz, J. Kucinska-Lipka, H. Janik, et al., Progress in used tyres management in the European Union: a review, Waste Manag. 32 (10) (2012) 1742–1751.
[2] H. Su, J. Yang, G.S. Ghataora, S. Dirar, Surface modified used rubber Tyre aggregates: effect on recycled concrete performance, Mag. Concr. Res. 67 (12) (2015) 680–691.
[3] M. Elzeadani, D.V. Bompa, A.Y. Elghazouli, Preparation and properties of rubberised geopolymer concrete: a review, Constr. Build. Mater. 313 (November) (2021), 125504, https://doi.org/10.1016/j.conbuildmat.2021.125504.
[4] S. Raffoul, D. Escolano-Margarit, R. Garcia, M. Guadagnini, K. Pilakoutas, Constitutive model for rubberized concrete passively confined with FRP laminates, J. Compos. Constr. 23 (6) (2019) 04019044, https://doi.org/10.1061/(ASCE)CC.1943-5614.0000972.
[5] D.V. Bompa, A.Y. Elghazouli, Stress–strain response and practical design expressions for FRP-confined recycled Tyre rubber concrete, Constr. Build. Mater. 237 (2020), 117633.
[6] K.S. Son, I. Hajirasouliha, K. Pilakoutas, Strength and deformability of waste tyre rubber-filled reinforced concrete columns, Constr. Build. Mater. 25 (1) (2011) 218–226, https://doi.org/10.1016/j.conbuildmat.2010.06.035.
[7] R. Hassanli, J.E. Mills, D. Li, et al., Experimental and numerical study on the behavior of rubberized concrete, Adv. Civ Eng. Mater. 6 (1) (2017) 134–156.
[8] R. Hassanli, O. Youssf, J.E. Mills, Experimental investigations of reinforced rubberized concrete structural members, J. Build. Eng. 31 (10) (2017) 149–165.
[9] O. Youssf, M.A. ElGawady, J.E. Mills, Experimental investigation of crumb rubber concrete columns under seismic loading, Structures 3 (2015) 13–27 [Elsevier].
[10] O. Youssf, M.A. ElGawady, J.E. Mills, Static cyclic behaviour of FRP-confined crumb rubber concrete columns, Eng. Struct. 15 (113) (2016) 371–387.
[11] A. Silva, Y. Jiang, J.M. Castro, N. Silvestre, R. Monteiro, Experimental assessment of the flexural behaviour of circular rubberized concrete-filled steel tubes, J. Constr. Steel Res. 122 (2016) 557–570, https://doi.org/10.1016/j.jcsr.2016.04.016.
[12] S. Khusru, D.P. Thambiratnam, M. Elchalakani, S. Fawzia, Experimental testing of novel hybrid rubberised concrete double skin tubular columns with filament wound CFRP tube under axial compressive loading, Compos. Struct. 276 (2021), 114568, https://doi.org/10.1016/j.compstruct.2021.114568.
[13] D.V. Bompa, A.Y. Elghazouli, Behaviour of confined rubberised concrete members under combined loading conditions, Mag. Concr. Res. (2019), https://doi.org/10.1680/jmacr.19.00121.
[14] A.Y. Elghazouli, D.V. Bompa, B. Xu, et al., Performance of rubberised reinforced concrete members under cyclic loading, Eng. Struct. 166 (2018) 526–545.
[15] A.P.C. Duarte, B.A. Silva, N. Silvestre, J. De Brito, E. Júlio, J.M. Castro, Tests and design of short steel tubes filled with rubberised concrete, Eng. Struct. 112 (2016) 274–286, https://doi.org/10.1016/j.engstruct.2016.01.018.
[16] S. Khusru, S. Fawzia, D.P. Thambiratnam, M. Elchalakani, Confined rubberised concrete tubular column for high-performance structures – review, Constr. Build. Mater. 276 (2021), 122216, https://doi.org/10.1016/j.conbuildmat.2020.122216.
[17] M. Nematzadeh, I. Hajirasouliha, A. Haghinejad, M. Naghipour, Compressive behaviour of circular steel tube-confined concrete stub columns with active and passive confinement, Steel Compos. Struct. 24 (3) (2017) 323–337, https://doi.org/10.12989/scs.2017.24.3.323.
[18] J.Y. Zhu, T.M. Chan, Experimental investigation on steel-tube-con-fined-concrete stub column with different cross-section shapes under uniaxial-compression, J. Constr. Steel Res. 162 (2019) 105729, https://doi.org/10.1016/j.jcsr.2019.105729.

[19] M. Elchalakani, M.F. Hassanein, A. Karrech, B. Yang, Experimental investigation of rubberised concrete-filled double skin square tubular columns under axial compression, Eng. Struct. 171 (2018) 730–746, https://doi.org/10.1016/j.engstruct.2018.05.123.
[20] M. Elchalakani, M.F. Hassanein, A. Karrech, S. Fawzia, B. Yang, V.I. Patel, Experimental tests and design of rubberised concrete-filled double skin circular tubular short columns, InStruct. 15 (2018) 196–210, https://doi.org/10.1016/j.istruc.2018.07.004.
[21] M. Dong, M. Elchalakani, A. Karrech, S. Fawzia, M.S.M. Ali, B. Yang, S.Q. Xu, Circular steel tubes filled with rubberised concrete under combined loading, J. Constr. Steel Res. 162 (2019) 105613, https://doi.org/10.1016/j.jcsr.2019.05.003.
[22] A. Mujdeci, D.V. Bompa, A.Y. Elghazouli, Confinement effects for rubberised concrete in tubular steel cross-sections under combined loading, Archives of Civil and Mechanical Engineering 21 (2) (2021), https://doi.org/10.1007/s43452-021-00204-8.
[23] A.P.C. Duarte, B.A. Silva, N. Silvestre, J. De Brito, E. Júlio, J.M. Castro, Experimental study on short rubberized concrete-filled steel tubes under cyclic loading, Compos. Struct. 136 (2016) 394–404, https://doi.org/10.1016/j.compstruct.2015.10.015.
[24] M.N.M.A. Mastor, M.A.A. Kadir, N. Zuhan, K.A. Mujedu, M.Z. Ramli, R.P. Jaya, N. M. Noor, M.S.A. Shah, Performance of rubberized concrete-filled hollow steel column under monotonic and cyclic loadings, Arch. Civ. Eng. (2022) 519–538.
[25] A. Silva, Y. Jiang, J.M. Castro, N. Silvestre, R. Monteiro, Monotonic and cyclic flexural behaviour of square/rectangular rubberized concrete-filled steel tubes, J. Constr. Steel Res. 139 (2017) 385–396, https://doi.org/10.1016/j.jcsr.2017.09.006.
[26] Abuzaid O, Nabilah AB, Safiee NA, Azline MN. (2019). Rubberized concrete filled steel tube. In: IOP Conference Series: Earth and Environmental Science (vol. 357 (1)). IOP Publishing; p.012014. Doi:https://doi.org/10.1088/1755-1315/357/1/012014.
[27] A.P.C. Duarte, B.A. Silva, N. Silvestre, J. de Brito, E. Júlio, J.M. Castro, Finite element modelling of short steel tubes filled with rubberized concrete, Compos. Struct. 150 (2016) 28–40, https://doi.org/10.1016/j.compstruct.2016.04.048.
[28] A.P.C. Duarte, N. Silvestre, J. de Brito, et al., Computational modelling of the cyclic behaviour of short rubberized concrete-filled steel tubes, Eng. Struct. 248 (2021) 113188.
[29] British Standard Institution, BS EN 197–1 Cement. Composition, Specifications and Conformity Criteria for Common Cements, BSI, London, 2011.
[30] British Standard Institution, BS EN 450–1, Fly Ash for Concrete, Part 1, Definition, Specifications and Conformity Criteria, BSI, London, 2013.
[31] D.V. Bompa, A.Y. Elghazouli, B. Xu, P.J. Stafford, A.M. Ruiz-Teran, Experimental assessment and constitutive modelling of rubberised concrete materials, Constr. Build. Mater. 137 (2017) 246–260.
[32] ECCS- TC1 – TWG 1.3, Recommended Testing Procedure for Assessing the Behavior of Structural Steel Elements under Cyclic Loads, ECCS, Brussels, 1986.
[33] L.H. Han, Flexural behaviour of concrete-filled steel tubes, J. Constr. Steel Res. 60 (2) (2004) 313–337.
[34] L.H. Han, W.D. Wang, Z. Tao, Performance of circular CFST column to steel beam frames under lateral cyclic loading, J. Constr. Steel Res. 67 (5) (2011) 876–890.
[35] A.Y. Elghazouli, J. Treadway, Inelastic behaviour of composite members under combined bending and axial loading, J. Constr. Steel Res. 64 (9) (2008) 1008–1019.
[36] British Standards Institutions, BS5400, Part 5, Steel, Concrete and Composite Bridges, 1979. London, UK.
[37] American Institute of Steel Construction (AISC), Specification for structural steel buildings, ANSI/AISC Standard 360-10, AISC, Chicago, Illinois, USA, 2010.
[38] CEN European Committee for Standardization, EN 1994-1-1 Eurocode 4: Design of Composite Steel and Concrete Structures – Part 1–1: General Rules and Rules for Buildings, British Standards, London, 2004.
[39] AIJ, Recommendations for Design and Construction of Concrete Filled Steel Tubular Structures, Architectural Institute of Japan (AIJ), Tokyo, Japan, 2008.
[40] ACI Committee, Building Code Requirements for Structural Concrete (ACI 318–08) and Commentary, American Concrete Institute, 2008.
[41] R.P. Johnson, Designers' Guide to Eurocode 4: Design of Composite Steel and Concrete Structures: EN 1994-1-1, ICE, London, 2012.
[42] A. Fam, F.S. Qie, S. Rizkalla, Concrete-filled steel tubes subjected to axial compression and lateral cyclic loads, J. Struct. Eng. 130 (4) (2004) 631–640.
[43] Y.F. An, L.H. Han, Behaviour of concrete-encased CFST columns under combined compression and bending, J. Constr. Steel Res. 101 (2014) 314–330.
[44] J.B. Mander, M.J.N. Priestley, R. Park, Theoretical stress–strain model for confined concrete, J. Struct. Eng. 114 (8) (1988) 1804–1826.
[45] CEN (European Committee for Standardization), EN 1992-1-1, Eurocode 2: Design of Concrete Structures, Part 1–1: General Rules for Buildings, CEN, Brussels (Belgium), 2004.
[46] A.Y. Elghazouli, A.S. Elnashai, Performance of composite steel/concrete members under earthquake loading. Part II: parametric studies and design considerations, Earthq. Eng. Struct. Dyn. 22 (4) (1993) 347–368, https://doi.org/10.1002/eqe.4290220405.
[47] M.A. Bradford, H.Y. Loh, B. Uy, Local Buckling of Concrete-Filled Circular Steel Tubes[M]//Composite Construction in Steel and Concrete IV, 2002, pp. 563–572.

Notations

β_c: Stiffness reduction factor
γ_{rcc}: Bending modification factor
δ_{buckle}: Buckling displacement
δ_C: Top horizontal displacement
δ_{frac}: Fracture displacement
δ_{Vpeak}: V_{peak} corresponding displacement
δ_{Mpeak}: M_{peak} corresponding displacement
δ_u: Ultimate displacement
δ_y: Yield displacement
ε_{c1}: Critical strain of the unconfined concrete
ε_{cc1}: Critical strain of the confined concrete
ε_{cr}: Critical buckling strain
ε_u: Ultimate strain
ε_y: Yield strain of steel
η: Slenderness factor
θ: Rotation of the vertical actuator
λ: Nondimensional slenderness
λ_{rcc}: Axially-loaded reduction factor
μ: Ductility index
ν: Poisson's ratio
ξ_D: Degradation modification factor
ρ_{vr}: Volumetric rubber ratio
φ: Curvature
χ_C: Load case modification factor
Δ: Drift ratio
Δ_u: Ultimate drift ratio
n_x: Axial load level
f_{cc}: Confined concrete strength
f_{rc} (f_c): Concrete cylinder compressive strength
$f_{rc,cube}$: Concrete cube compressive strength
f_s: Yield stress of steel
f_u: Ultimate stress of steel
h_n: Distance between axes
k_p: Predicted member stiffness
k_{test}: Testing member stiffness
t: Thickness
v_a: Axial load ratio
A: Section area
D: Diameter of the specimen
E: Elastic modulus
H_n: Neutral axis depth
I: Second area moment
L_c: Length of the specimen
L_d: Distance between the member top and the lower vertical hinge
L_p: Plastic hinge length
L_t: Distance between the vertical hinges
M: Moment
M_{peak}: Maximum moment
$M_{P-\Delta}$: Second order moment
M_y: Yield moment
N or P: Vertical / axial load
V_A: Horizontal force from the actuator
V_H: Overall horizontal force
V_{peak}: Maximum horizontal force
V_y: Yield horizontal force
W: Section modulus